PAPER

La$_{1-x}$Ag$_x$MnO$_3$ electrocatalyst with high catalytic activity for oxygen reduction reaction in aluminium air batteries

Yejian Xue, He Miao,* Shanshan Sun, Qin Wang, Shihua Li and Zhaoping Liu*

The LaMnO$_3$ (LMO) perovskite catalyst has been proposed as one of the best oxygen reduction reaction catalysts (ORRCs) to substitute noble metals. However, its ORR catalytic activity needs to be further improved. Here, La$_{1-x}$Ag$_x$MnO$_3$ (LAM) perovskites doped with Ag are synthesized by a facile improved sol–gel method. The structures, morphologies and valence states of Mn and oxygen adsorption behaviors of these LAM samples are characterized, and their catalytic activities toward ORR are studied by the rotating ring-disk electrode (RRDE) and aluminum air battery technologies. The results demonstrate that the doping of 30% Ag in the A-site of LMO (LAM-30) can effectively improve its ORR catalytic activity due to the regulation of the manganese valence and improvement of the oxygen adsorption capacity. Besides the remarkable ORR catalytic activity, the LAM-30 catalyst exhibits good durability. The current retention is as high as 98% after the aging test for 10 000 seconds. In addition, the maximum power density of the aluminum air battery using LAM-30 as the ORRC can reach 230.2 mW cm^{-2}, which indicates that LAM-30 can be used as a promising ORRC in aluminum air batteries.

1. Introduction

Metal–air batteries have received particular attention due to their high energy density, environmental friendliness and low cost.[1–3] Aluminium (Al) is an attractive candidate anode material for metal–air batteries because it has a high theoretical electrochemical equivalent value of 2.98 A h g^{-1}, which is higher than that of most metal anodes, such as magnesium (2.20 A h g^{-1}) and zinc (0.82 A h g^{-1}).[3] The Al–air battery is mainly composed of the aluminium anode, aqueous electrolyte, air-breathing cathode and oxygen reduction reaction catalyst (ORRC).[1,4] Among them, the ORRC is one of the most critical components due to the sluggish oxygen reduction reaction (ORR).[5–7] Therefore, developing a cost-effective ORRCs is of importance in facilitating the commercial application of the metal–air batteries.

Recently, some perovskite materials have been proposed as one of the promising ORRCs to substitute the Pt/C catalyst.[8–13] Among them, the LaMnO$_3$ is one of the most widely-applied ORRCs in fuel cells or metal–air batteries.[14–19] It has been reported that the substitution of La with the low valence state metal can further improve the catalytic activity of LaMnO$_3$, which can be related to the modification of the perovskite band structure and manipulation of manganese valence state between Mn^{3+} and Mn^{4+}.[8,14,20]

In addition, silver also has been identified as one of the most promising ORRC because it is about 50 times cheaper than Pt, highly stable and reasonably active towards ORR in the alkaline solutions.[21–23] Recently, some papers[23–26] have reported that compositing with the metal oxides can promote the electron-depleted Ag to be oxidized to Ag$_2$O film because of the strong electronic affinity. The monolayer Ag$_2$O film formed on the Ag surface which contains a large number of active sites can effectively improve the ORR catalytic activities of Ag.[23]

By integrating the merits of both Ag and LaMnO$_3$, the Ag/LaMnO$_3$ composite catalysts show a much higher ORR activity than LaMnO$_3$ or Ag in the alkaline media.[27,28] Whereas, to the best of our knowledge, the investigation on the Ag-doped LaMnO$_3$ perovskite as the ORRC has not been reported, though it has been widely applied as the solid oxide fuel cell cathode, NO oxidation catalyst and electromagnetic material.[29–42]

In this work, a series of La$_{1-x}$Ag$_x$MnO$_3$ ($x = 0$, 0.15, 0.3 and 0.45) perovskites were prepared by an improved sol–gel method. And the La$_{0.7}$Ag$_{0.3}$MnO$_3$ exhibits the optimal catalytic activity toward ORR, which can be ascribed to the regulation of Mn valence state and improvement of the oxygen absorption ability by the substitution of Ag. By applying La$_{0.7}$Ag$_{0.3}$MnO$_3$ as ORRC, the maximum power density of Al–air battery can reach 230.2 mW cm^{-2}.

2. Experimental

2.1 Material preparation and characterization

The La$_{1-x}$Ag$_x$MnO$_3$ ($x = 0$, 0.15, 0.3 and 0.45) (LAM) powders were prepared by an improved sol–gel method.[43] High-purity

Advanced Li-ion Battery Engineering Laboratory, Key Laboratory of Graphene Technologies and Applications of Zhejiang Province, Ningbo Institute of Materials Technology & Engineering, Chinese Academy of Sciences, Zhejiang 315201, P. R. China. E-mail: miaohe@nimte.ac.cn; liuzp@nimte.ac.cn

lanthanum acetate, manganese acetate, silver nitrate and citric acid purchased from Sinopharm Chemical Reagent Co. Ltd. were used as starting materials without further purification. The above starting materials were mixed in the aqueous solution by gentle stirring with the stoichiometric ratio of the $La_{1-x}Ag_xMnO_3$ ($x = 0$, 0.15, 0.3 and 0.45), respectively. The amount of citric acid with the mole ratio to overall metal ions of 2 was added into the solution. Then, the solution was kept in a water bath at 80 °C with the constant stirring till the gel was completed. Then, the gel was dried at 180 °C for 24 hours. Finally, the LAM powders were obtained by the calcination of the dried gels at 700 °C for 2 h. In this paper, the samples of $La_{1-x}Ag_xMnO_3$ ($x = 0$, 0.15, 0.3 and 0.45) were abbreviated as LAM-0, LAM-15, LAM-30, LAM-45, respectively. For comparison, the $La_{0.7}Sr_{0.3}MnO_3$ (LSM-30) was prepared by the almost same method, and the strontium nitrate was used as the strontium solution. The Ag powder with the diameter of 60 nm was used as the benchmark and purchased from Sinopharm Chemical Reagent Co. Ltd.

The phase identifications of the different samples were characterized by X-ray diffraction (XRD, D8 Advance, Bruker AXS) with a Cu K_α radiation source at a step of 0.02° in the range of 2θ from 20° to 80°. The compositions of the different samples were examined by X-ray fluorescence (XRF, ZSX Primus II, Rigaku). The morphologies of the samples were investigated by the field-emission scanning electron microscopy (SEM, FEI Quanta FEG 250) and transmission electron-microscopy (TEM, JEOL-2100). The valence states of manganese and silver as well as the oxygen species of the different perovskite powders were measured by the X-ray photoelectron spectroscopy (XPS, AXIS ULTARDLD) with Al-Kα (1486.6 eV) radiation.

The oxygen adsorption behaviours of the different perovskite powders were also measured by Temperature Programmed Desorption (TPD, AutoChem II 2920, Micromeritics). Specifically, the perovskite powder (about 200 mg) placed in a quartz reactor was pre-treated in the 3%O$_2$/He mixed gas (50 sccm) at the temperature of 120 °C for 1 hour to remove the dissociative water. Subsequently, the sample was cooled down to room temperature and then heated to 900 °C (5 °C min^{-1}) in He atmosphere (50 sccm).

2.2 Electrochemical measurement

The ORR activities of the different catalysts were studied by the rotating ring-disk electrode (RRDE) (E7R9, Pine) technique. The RRDE measurements were performed by a three-electrode system in 0.1 M KOH. The Pt wire and Hg/HgO electrode were served as the counter and reference electrode, respectively. The working electrode was a catalyst-coated RRDE (Pt ring and glass carbon (GC) disk, disk diameter: 5.6 mm, ring: 6.25–7.92 mm, current collection efficiency: 37%). The disk potential was scanned from 1.1 to 0.1 V (*vs.* RHE) at the scan rate of 5 mV s^{-1}, and the potential of Pt ring electrode was held at 1.4 V (*vs.* RHE).[44] Prior to the measurement, O$_2$ was bubbled directly into the electrolyte solution for at least 30 minutes to saturate the solution, and the O$_2$ atmosphere was maintained during the electrochemical measurements. The catalyst ink was made from a suspension of
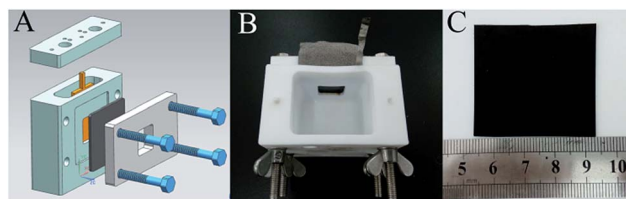

Fig. 1 Diagram of the homemade testing device (A), testing house (B), and the cathode electrode (C).

the catalyst, Vulcan XC-72, 160 μL of Nafion solution (5 wt%) and 2 mL of alcohol. The amount of the catalyst and VXC-72 was same, being 10 mg. Then, the suspension was dispersed by the ultrasound method for 30 minutes. Finally, 12.5 μL ink was dropped onto the glassy carbon working electrode and the catalyst loading was approximately 0.236 mg cm^{-2}.

2.3 Aluminium air battery test

Aluminium–air batteries were fabricated for testing the power densities on a multichannel battery testing system (CT2001A, Land Company) at about 30 °C. The as-synthesized LAM-0, LAM-30, LSM-30 and the Ag were used as the ORR catalysts. The cathodes were fabricated with a three-layer structure including the catalytic layer, gas diffusion layer and current collector layer. The current collector layer and gas diffusion layer were nickel foam and porous PTFE film with a square area (4 cm × 4 cm), respectively. The catalytic layer was prepared by the following sequence: (i) as-prepared catalyst (0.36 g) and VXC-72 (0.36 g) were mixed in 50 ml ethanol to obtain a homogeneous solution and then the solution was stirred magnetically in a beaker; (ii) 0.5 g PTFE emulsion (60 wt%) was added into the solution and stirred for further 30 minutes; (iii) the beaker was then transferred into an 80 °C water-bath with stirring until the ethanol was evaporated and the slurry formed a paste; (iv) the paste was rolled into a 0.35 mm of film with a square area of 4 cm × 4 cm. The catalytic layer was placed on the nickel foam, and pressed with a pressure of 20 MPa for 2 minutes, followed by the sintering at 340 °C for 30 minutes. Then, the above two-layer architecture was placed on the porous PTFE film, and pressed with a pressure of 10 MPa for 2 minutes at 150 °C. Aluminium–air batteries were fabricated by using the as-prepared air cathodes and tested by a homemade testing device (PTFE material) (shown in Fig. 1). A high pure aluminium (99.99%) with an active area of 2 × 2 cm^2 and 4 mol L^{-1} KOH aqueous solution were used as the anode and electrolyte, respectively. All aluminum–air batteries were tested in normal atmospheric environment using air as reactants.

3. Results and discussion

The X-ray diffraction patterns of the different perovskites are shown in Fig. 2A. XRD results confirm the formation of the perovskite phase (PDF: 051-0409 and 054-1275) for all the LAM and LSM samples synthesized in this work. Almost no Ag metal (PDF: 04-0783) can be detected in the LAM-15 and LAM-30

samples. However, the Ag metal is observed in the LAM-45 sample as an impurity phase, indicating the limited solubility of Ag in LaMnO$_3$.

In order to further confirm that the Ag has been successfully doped in the LAM samples, the XPS spectrum of the Ag 3d levels of the different catalysts are measured and shown in Fig. 2B. As shown in Fig. 1B, the binding energies of the Ag 3d$_{5/2}$ for the pure Ag, LAM-15, LAM-30 and LAM-45 are 368.2 eV, 367.6 eV, 367.6 eV and 368.1 eV, respectively. According to the ref. 25 and

45, the silver species in the LAM-15 and LAM-30 are mainly Ag$^+$, while the metal Ag and Ag$^+$ coexist in the LAM-45 sample. This result is in accordance with that from XRD measurements. In addition, all the powders are examined by X-ray fluorescence (XRF), and the results confirm the target compositions. Nitrogen adsorption–desorption measurements were carried out (shown in Fig. 2C). The BET surface areas of LAM-0, LAM-15, LAM-30, LAM-45 and LSM-30 are 21.4, 20.5, 19.1, 20.1 and 19.3 m^2 g^{-1}, respectively.

Fig. 3 shows the SEM and TEM images of LAM-30 as a representative sample. As can be seen from Fig. 3, the LAM-30 powder synthesized at 700 °C aggregates slightly with the average particle size being about 150 nm. Fig. 4A shows the CV curves of the LAM-0, LAM-15, LAM-30, LAM-45, LSM-30 and Ag. For the six samples, the reduction peaks are negligible in the N$_2$-saturated solution (dashed line), while the obvious reduction peaks of the samples appear from 0.59 V to 0.79 V in the O$_2$-saturated solution (solid line). Among them, the LAM-30 shows the most positive reduction peak appearing at 0.79 V with the highest peak current density of 0.57 mA cm^{-2} (all ORR current densities were normalized by the area of disk). These results demonstrate the high catalytic activity of LAM-30 toward ORR. Fig. 4B shows the disk current density (i_d) and ring current (i_r) collected on the different catalysts during ORR in O$_2$-saturated KOH solution (0.1 mol L^{-1}) at a rotation rate of 1600 rpm. Obviously, the onset potential (the potential at 100 μA cm^{-2})[46,47] of the LAM catalysts increases from 0.787 V (*vs.* RHE, LAM-0) to 0.959 V (*vs.* RHE, LAM-30), and then decreases to 0.887 V (*vs.* RHE, LAM-45) with the increase of the Ag content. In addition, with the substitution of La by Ag, the half-wave potential ($E_{1/2}$) shows the same variation tendency with the onset potential. Also, the onset potential and half-wave potential of LAM-30 are much more positive than those of the Ag and LSM-30 catalysts. It is well believed that the ring current is an important parameter to evaluate the ORR catalytic activity of ORRCs. From Fig. 4B, the LAM-30 catalyst presents the lowest ring current among the six samples at the whole scanning potential.

Fig. 4C shows the LSV curves of the LAM-30 composite catalyst at the rotation rate from 100 to 2400 rpm. Obviously, the ORR operates under a mixed kinetic-diffusion controlled regime in the potential range from 0.8 V to 0.4 V (*vs.* RHE). The K–L plots can be expressed by the following eqn (1) and (2):[18,48]
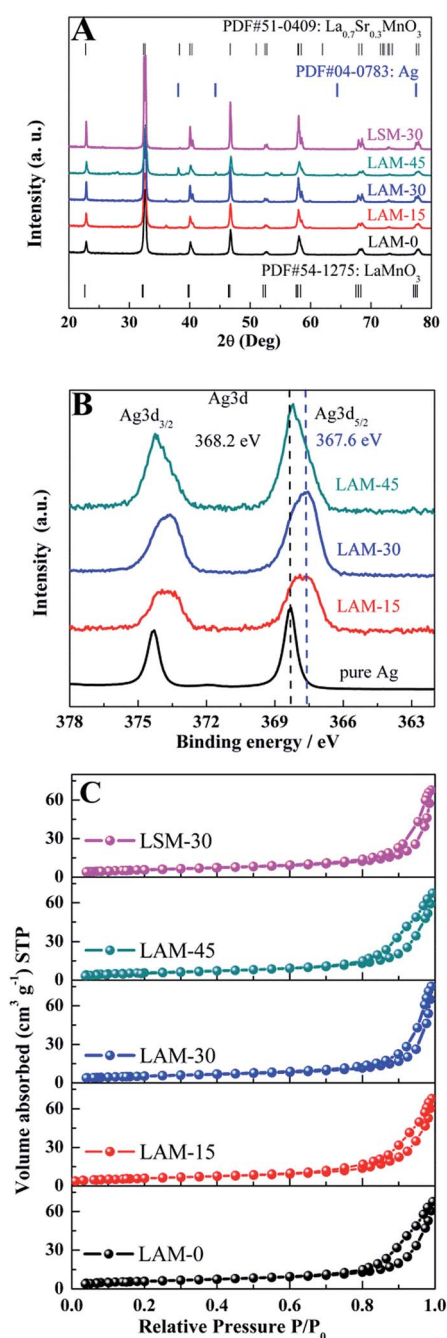

Fig. 2 XRD patterns of the different perovskite catalysts (A), XPS spectrums of the Ag 3d levels of the different catalysts (B), and nitrogen adsorption–desorption isotherms (C) of the different perovskite catalysts.
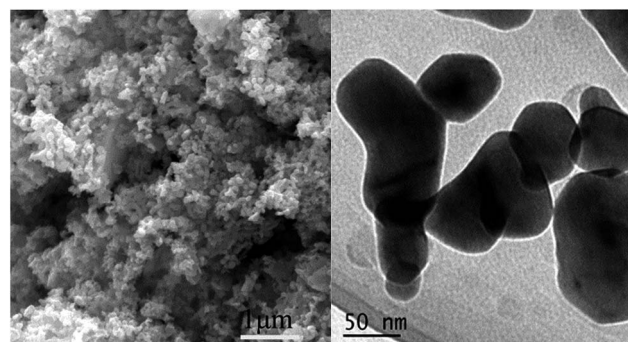

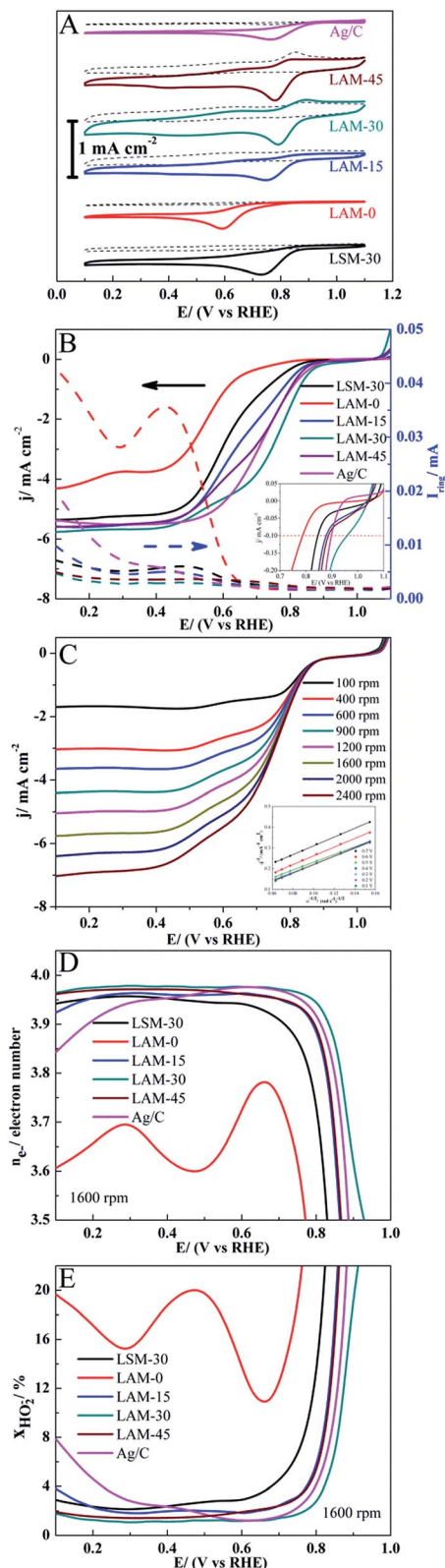**Fig. 3** Representative SEM and TEM micrographs of the LAM-30.

Fig. 4   ORR catalytic activities of the different perovskite catalysts: CV curves (A); RRDE polarization curves at the rotation rate of 1600 rpm (B); LSV curves of the LAM-30 sample at the different rotation rates (C); overall number of transferred electrons (n_{e^-}) (D) and mole content of the HO_2^- species for the different LSM samples in the scanning potential range from 0.8 V to 0.1 V (vs. RHE) (E).

$$i^{-1} = i_L^{-1} + i_K^{-1} = (B\omega^{1/2})^{-1} + i_K^{-1} \tag{1}$$

$$B = 0.62nFC_0(D_0)^{2/3}\nu^{-1/6} \tag{2}$$

where i is the measured current density; i_K and i_L are the kinetic and diffusion-limiting current densities, respectively; ω is the angular velocity of the disk, n is the overall number of electrons transferred in the oxygen reduction; F is the Faraday constant (96 485 C mol^{-1}); C_0 is O$_2$ volume concentration (1.2 $\times$ 10^{-6} mol cm^{-3}); ν is the kinematic viscosity of the electrolyte (0.01 cm^2 s^{-1}); and D_0 is the diffusion coefficient of O$_2$ in 0.1 M KOH (1.9 $\times$ 10^{-5} cm^2 s^{-1}). The electron transferred number of LAM-30 calculated from the K–L equations is about 3.96–4, which confirms that the ORR mechanism on this LAM catalyst is an apparent 4 electron reaction path.

From the RRDE measurement, the percentage of formed peroxides (HO_2^-) with respect to the total oxygen reduction products ($\chi_{HO_2^-}$) and the electron transferred number (n_{e^-}) can be calculated by the disk current (I_{disk}), ring current (I_{ring}) and ring collection efficiency (N) with the eqn (3) and (4), respectively.[49]

$$\chi_{HO_2^-} \, [\%] = 100 \frac{2I_{ring}/N}{I_{disk} + I_{ring}/N} \tag{3}$$

$$n_{e^-} = \frac{4NI_{disk}}{NI_{disk} + I_{ring}} \tag{4}$$

Fig. 4D and E show the relations of n_{e^-} and $\chi_{HO_2^-}$ with the scanning potential from 0.8 V to 0.1 V (vs. RHE). The overall electron transferred numbers (n_{e^-}) for the LAM-30 are larger than 3.95 during the whole scanning potential range, and present the highest values among the six samples. This further confirms that the ORR mechanism on LAM-30 catalyst is an apparent 4 electron reaction path. Comparing with n_{e^-}, $\chi_{HO_2^-}$ for the different samples almost show an inverse variation tendency in the same scanning potential range (Fig. 4E). The n_{e^-} and $\chi_{HO_2^-}$ for the six different catalysts at the half-wave potential ($E_{1/2}$) and 0.4 V (vs. RHE, in the gas diffusion control region) are summarized in Table 1. Obviously, the LAM-30 catalyst presents the highest n_{e^-} and lowest $\chi_{HO_2^-}$ at these potentials.

From the results of the onset potential, half-wave potential, electron transferred number (n_{e^-}) and percentage of the formed peroxides ($\chi_{HO_2^-}$), it can be concluded that the LAM-30 presents the best ORR catalytic activity among all the LAM perovskites and the benchmarks of LSM-30 and Ag. Furthermore, in terms of the onset potential and half-wave potential, the ORR catalytic activity of LAM-30 surpasses that of the most of LSM or Ag/LaMnO$_3$ composite catalysts reported in the ref. 27, 28 and 59 (shown in Table 1), which indicates that Ag doping is one of the best methods for improving the catalytic activity of the LaMnO$_3$ perovskites. For further clarifying the catalytic mechanism of LAM-30 toward ORR, the Tafel curves, XPS spectrum and oxygen desorption behaviours are analysed.

The Tafel curves for the LAM-0, LAM-30, LSM-30 and Ag catalysts in the potential region from 0.78 to 0.88 V (vs. RHE) are shown in Fig. 5A. The Tafel slope is generally explained with

Table 1 Onset potentials, half-wave potentials, n_{e^-} and mole content of the HO_2^- species of the different catalysts[a]

Sample	$E_{onset\ potential}$ (V) (1600 rpm, 100 $\mu A\ cm^{-2}$)	$E_{1/2}$ (V) (1600 rpm)	$n_{e^-(E_{1/2})}$ (1600 rpm, disk-ring)	$HO_2^-\%_{(E_{1/2})}$ (1600 rpm, disk-ring)	$n_{e^-(0.4\ V)}$ (1600 rpm, disk-ring)	$HO_2^-\%_{(0.4\ V)}$ (1600 rpm, disk-ring)	References
LSM-30	0.846	0.610	3.94	2.98	3.95	2.37	This work
LAM-0	0.787	0.543	3.64	18.08	3.62	18.75	This work
LAM-15	0.878	0.649	3.96	2.04	3.96	1.97	This work
LAM-30	0.959	0.749	3.97	1.72	3.98	1.12	This work
LAM-45	0.887	0.704	3.95	2.44	3.97	1.43	This work
Ag	0.899	0.718	3.96	1.73	3.95	2.34	This work
Ag/C	0.80	0.672	3.79	10.51	3.82	8.92	26
Ag/LaMnO$_3$	0.85	0.725	3.98	0.77	3.71	14.60	26
Ag/LaMnO$_3$-RGO	0.81	0.58	3.98	1.02	3.97	1.82	27
La$_{0.4}$Sr$_{0.6}$MnO$_3$	0.765	0.465	—	—	—	—	58
LaMnO$_3$	—	0.82	3.8[b]	—	3.8[b]	—	59
La$_{0.8}$Sr$_{0.2}$MnO$_3$	0.868	0.628	—	—	—	—	60
La$_{0.8}$Sr$_{0.2}$MnO$_3$ nanorod	0.834	0.660	—	—	—	—	61

[a] All potentials are reported (V vs. RHE) by making appropriate conversions.[51] [b] Determined from the slope of Koutecky–Levich plots.

respect to the coverage degree of adsorbed oxygen and calculated from the Tafel equation.[50,51] The Tafel slopes of the LAM-0, LAM-30, LSM-30 and Ag are -87, -83, -85 and $-97\ mV\ dec^{-1}$, respectively. It is worth noting that the LAM-30 displays the smallest Tafel slope among the four samples, which can be related to its high coverage degree of the adsorbed oxygen.[50,52] Fig. 5B shows the mass specific activities of the different catalysts at the potential of 0.7 V and 0.8 V, respectively. Obviously, the mass specific activity of LAM-30 can reach 48.0 $mA\ mg^{-1}$ (0.7 V), which is about 32 times that of LAM-0.
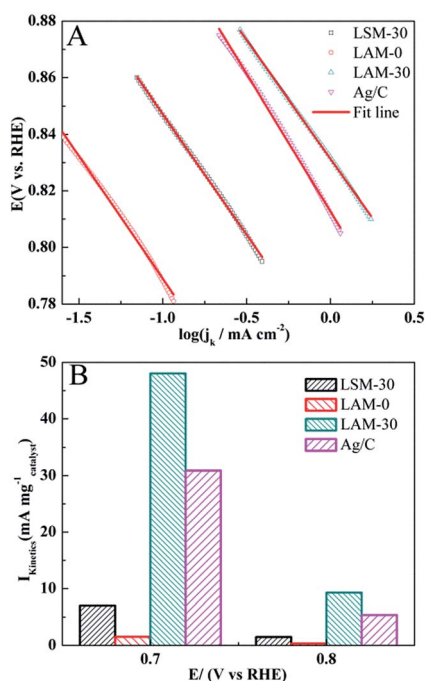
From Fig. 6A, the two Mn 2p peaks located at 642 and 653 eV can be attributed to Mn $2p_{3/2}$ and Mn $2p_{1/2}$ spin–orbit doublet, respectively. The Mn $2p_{3/2}$ peak is separated into two peaks at 640.8 and 642.3 eV, corresponding to Mn^{3+} and Mn^{4+}, respectively.[55] By simulation, the contents of Mn^{3+} and Mn^{4+} are obtained and listed in Table 2. The mass percent of Mn^{4+} in the LAM perovskite increases from 19.6% (LAM-0) to 49.9% (LAM-30), while that of Mn^{3+} decreases from 80.4% (LAM-0) to 50.1% (LAM-30) with the increase of Ag content. In addition, comparing with LSM, the mass percent of Mn^{4+} in the LAM-30 is much higher. This indicates that the doping of monovalent Ag with the content of 30% in the LaMnO$_3$ can effectively tailor the Mn valence of LAM, and the proper mass ratio of Mn^{3+}/Mn^{4+} (about 1) is beneficial to the catalytic activity of the LMO perovskite, which is consistent with the results of the doping of 60% bivalent Sr in the LaMnO$_3$ catalyst.[58]

The XPS spectra of the O 1s levels of the LAM-0, LAM-30 and LSM-30 catalysts are shown in Fig. 6B. The XPS peaks for O 1s are identified at the binding energies of about 529.3, 531.2 and 533.2 eV corresponding to the lattice oxygen on the surface of the perovskite (O_{latt}), surface adsorbed oxygen species (O_{ads}) and oxygen in the molecular water adsorbed on the catalyst
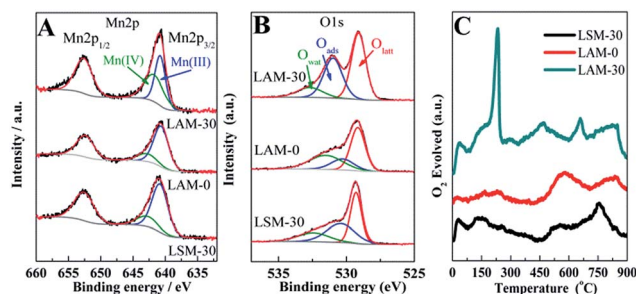

Fig. 5 Tafel curves (A) and mass specific activities (B) of the different samples.

Fig. 6 XPS spectrums of the Mn 2p (A) and O 1s (B) levels and oxygen TPD patterns (C) of the different perovskite catalysts.

Table 2 Manganese valences, oxygen species and O_2 desorption contents of the different perovskite catalysts

Sample	Mn^{3+} (%)	Mn^{4+} (%)	H_2O (XPS-O 1s) (%)	O_{ads} (XPS-O 1s) (%)	O_{latt} (XPS-O 1s) (%)	O_{ads}/O_{latt}	O_2 desorption ($\mu mol\ g^{-1}$)
LSM-30	77.8	22.2	19.6	32.5	47.9	0.68	144.6
LAM-0	80.4	19.6	34.8	18.6	46.6	0.40	54.7
LAM-30	50.1	49.9	8.4	44.6	47.0	0.95	295.5

surface (O_{wat}, H_2O), respectively.[30,53,54] The relative ratios of the three O 1s XPS peak intensities are obtained from the deconvolution of the peaks. The mass percent of the different oxygen species are summarized in Table 2. The LAM-30 has the highest mass percent of the O_{ads} (44.6%) among the three samples. The O_{ads}/O_{latt} ratio of the LAM-30 (0.95) is also much higher than those of the LSM-30 (0.68) and LAM-0 (0.4) catalysts. This means that the doping of Ag is beneficial to the oxygen adsorption behaviours of the LMO catalysts.

In order to further study the oxygen adsorption behaviours, the oxygen TPD patterns of the three perovskites are measured and depicted in Fig. 6C. All the samples show the very intense TPD peaks in the temperature range from 100 °C to 400 °C, which can be attributed to the readily oxygen desorption from the catalyst surface.[30,53] From Fig. 6C, the LAM-30 sample has the highest O_2 desorption content (295.5 $\mu mol\ g^{-1}$), which is favour to catalyse ORR.[51,53,55–57] The results from Tafel curves, XPS and TPD measurements demonstrate that the improvement of the ORR catalytic activities of the LMO perovskite with the doping of Ag can be ascribed to the increase of the oxygen adsorption ability.

For evaluating the durability, the stabilities of the LAM-30 and Ag are measured by the chronoamperometric measurement at 0.4 V (vs. RHE) in O_2-saturated 0.1 M KOH at the rotating rate of 1600 rpm for 10 000 seconds. As can be seen in Fig. 7, both LAM-30 and Ag show a slight degradation and their current retentions are as high as 98% after 10 000 s. In addition, the $\chi_{HO_2^-}$ derived from the RRDE measurement in O_2-saturated 0.1 M KOH at 1600 rpm are also recorded during the degradation test. Obviously, for Ag, the HO_2^- increases slightly from
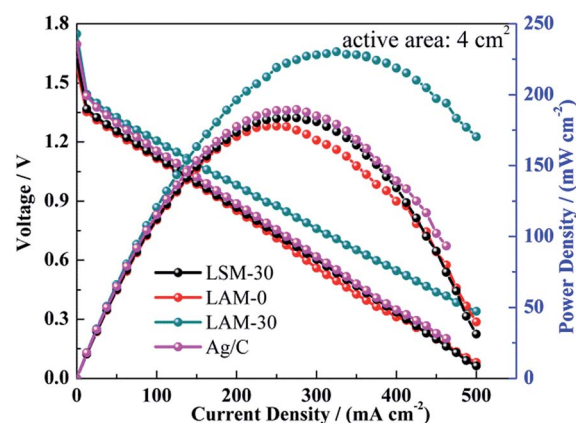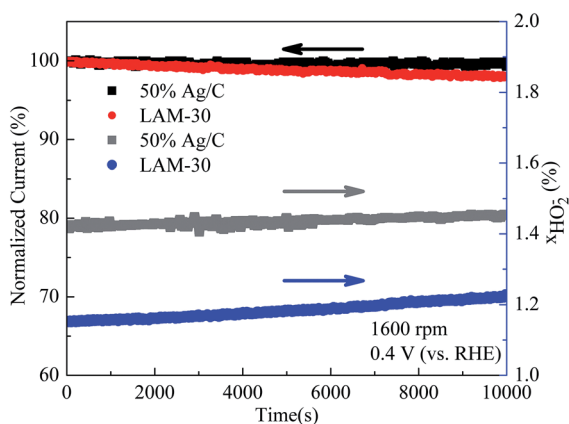

Fig. 8 $I–V/I–P$ curves of the aluminium air batteries with the different ORRCs.

1.41% to 1.46% after 10 000 s. Whereas, comparing with Ag, the LAM-30 generates even less HO_2^- (1.15–1.22%) during the whole aging process. This means that the stability of LAM-30 is comparable to that of Ag/C.

For further evaluating the catalytic activities of the different catalysts, the aluminium air batteries using LAM-0, LAM-30, LSM-30 and Ag as the ORRCs are measured, and their $I–V/I–P$ curves are shown in Fig. 8. The maximum power density (P_{max}) of the battery using high pure aluminium (99.99%) as the anode with LAM-30 catalyst can reach 230.2 mW cm^{-2}, which is the highest among the four batteries. The P_{max} is higher than that of battery with polytetraphenylporphyrin iron(II) (40.5 mW cm^{-2}),[62] N-doped porous carbon (150 mW cm^{-2}),[63] and Ag–MnO_2 (204 mW cm^{-2})[64] as the cathode catalyst using high pure aluminium as the anode. It is close to that of the battery with Ag/N-RGO (268 mW cm^{-2})[65] and polyacrylonitrile-based catalysts (300 mW cm^{-2})[66] as the cathode catalyst using Al–Mg–Sn–Ga and Al–In alloy as the anode, respectively. This confirms that the proper doping of Ag in the $LaMnO_3$ perovskite is beneficial to its ORR catalytic activity.

4. Conclusions

In summary, the Ag was successfully doped in the $La_{1-x}Ag_x$-MnO_3 (LAM) perovskites by an improved sol–gel method. Among all the LAM samples in this work, the $La_{0.7}Ag_{0.3}MnO_3$ (LAM-30) exhibits the best ORR catalytic activity, and it is also superior to that of LSM-30 and Ag. The onset potential, half-wave potential and electron transfer number of LAM-30

Fig. 7 Durability and percentages of the peroxides ($\chi_{HO_2^-}$) during the degradation test of the LAM-30 and Ag catalysts.

correspond to 0.959 V, 0.749 V and 3.97, respectively. The remarkable ORR catalytic activity of LAM-30 can be related to the regulation of the Mn valence and improvement of the oxygen adsorption capacity with the appropriate doping of Ag. Also, the LAM-30 catalyst has a good durability with the current retention of 98% after 10 000 s. The maximum power density of the aluminium air battery using LAM-30 as the ORRC can reach 230.2 mW cm^{-2}. The results of this paper indicate that the Ag-doped LAM catalysts can be used as a promising ORRCs for the aluminium air batteries.

Acknowledgements

Notes and references

1 F. Cheng and J. Chen, *Chem. Soc. Rev.*, 2012, **41**, 2172–2192.
2 Y. Li and H. Dai, *Chem. Soc. Rev.*, 2014, **43**, 5257–5275.
3 M. Mokhtar, M. Z. M. Talib, E. H. Majlan, S. M. Tasirin, W. M. F. W. Ramli, W. R. W. Daud and J. Sahari, *J. Ind. Eng. Chem.*, 2015, **32**, 1–20.
4 L. D. Chen, J. K. Norskov and A. C. Luntz, *J. Phys. Chem. Lett.*, 2015, **6**, 175–179.
5 M. Armand and J. M. Tarascon, *Nature*, 2008, **451**, 652–657.
6 K. A. Stoerzinger, W. Lu, C. Li, Ariando, T. Venkatesan and Y. Shao-Horn, *J. Phys. Chem. Lett.*, 2015, **6**, 1435–1440.
7 T. Li, J. Liu, X. Jin, F. Wang and Y. Song, *Electrochim. Acta*, 2016, **198**, 115–126.
8 J. Suntivich, H. A. Gasteiger, N. Yabuuchi, H. Nakanishi, J. B. Goodenough and Y. Shao-Horn, *Nat. Chem.*, 2011, **3**, 546–550.
9 J. Suntivich, H. A. Gasteiger, N. Yabuuchi and Y. Shao-Horn, *J. Electrochem. Soc.*, 2010, **157**, B1263.
10 T. Poux, F. S. Napolskiy, T. Dintzer, G. Kéranguéven, S. Y. Istomin, G. A. Tsirlina, E. V. Antipov and E. R. Savinova, *Catal. Today*, 2012, **189**, 83–92.
11 T. Poux, A. Bonnefont, G. Kerangueven, G. A. Tsirlina and E. R. Savinova, *ChemPhysChem*, 2014, **15**, 2108–2120.
12 K. Miyazaki, K.-i. Kawakita, T. Abe, T. Fukutsuka, T. Kojima and Z. Ogumi, *J. Mater. Chem.*, 2011, **21**, 1913–1917.
13 S. Malkhandi, P. Trinh, A. K. Manohar, K. C. Jayachandrababu, A. Kindler, G. K. Surya Prakash and S. R. Narayanan, *J. Electrochem. Soc.*, 2013, **160**, F943–F952.
14 M. Risch, K. A. Stoerzinger, S. Maruyama, W. T. Hong, I. Takeuchi and Y. Shao-Horn, *J. Am. Chem. Soc.*, 2014, **136**, 5229–5232.
15 K. A. Stoerzinger, M. Risch, J. Suntivich, W. M. Lü, J. Zhou, M. D. Biegalski, H. M. Christen, Ariando, T. Venkatesan and Y. Shao-Horn, *Energy Environ. Sci.*, 2013, **6**, 1582.
16 F. Lu, J. Sui, J. Su, C. Jin, M. Shen and R. Yang, *J. Power Sources*, 2014, **271**, 55–59.
17 C. Jin, X. Cao, L. Zhang, C. Zhang and R. Yang, *J. Power Sources*, 2013, **241**, 225–230.
18 Y. J. Xue, H. Miao, C. R. He, J. X. Wang, M. Liu, S. S. Sun, Q. Wang and W. G. Wang, *J. Power Sources*, 2015, **279**, 610–619.
19 V. Celorrio, E. Dann, L. Calvillo, D. J. Morgan, S. R. Hall and D. J. Fermin, *ChemElectroChem*, 2016, **3**, 283–291.
20 J. Suntivich, K. J. May, H. A. Gasteiger, J. B. Goodenough and Y. Shao-Horn, *Science*, 2011, **334**, 1383–1385.
21 Y. Cheng, Y. Tian, S.-W. Tsang and C. Yan, *Electrochim. Acta*, 2015, **174**, 919–924.
22 X. Wu, F. Chen, N. Zhang, A. Qaseem and R. L. Johnston, *J. Mater. Chem. A*, 2016, **4**, 3527–3537.
23 J. Liu, J. Liu, W. Song, F. Wang and Y. Song, *J. Mater. Chem. A*, 2014, **2**, 17477–17488.
24 J. S. Guo, A. Hsu, D. Chu and R. R. Chen, *J. Phys. Chem. C*, 2010, **114**, 4324–4330.
25 J. Ohyama, Y. Okata, N. Watabe, M. Katagiri, A. Nakamura, H. Arikawa, K.-i. Shimizu, T. Takeguchi, W. Ueda and A. Satsuma, *J. Power Sources*, 2014, **245**, 998–1004.
26 T. Van Cleve, E. Gibara and S. Linic, *ChemCatChem*, 2016, **8**, 256–261.
27 S. A. Park, E. K. Lee, H. Song and Y. T. Kim, *Sci. Rep.*, 2015, **5**, 13552.
28 J. Hu, L. Shi, Q. Liu, H. Huang and T. Jiao, *RSC Adv.*, 2015, **5**, 92096–92106.
29 Y. Zhu, W. Zhou, R. Ran, Y. Chen, Z. Shao and M. Liu, *Nano Lett.*, 2016, **16**, 512–518.
30 D. Y. Yoon, E. Lim, Y. J. Kim, J. H. Kim, T. Ryu, S. Lee, B. K. Cho, I.-S. Nam, J. W. Choung and S. Yoo, *J. Catal.*, 2014, **319**, 182–193.
31 Y. Kalyana Lakshmi, N. Pavan Kumar and P. Venugopal Reddy, *J. Supercond. Novel Magn.*, 2013, **26**, 2975–2980.
32 Q. Wu, L. Zhao, J. Wu and W. Yao, *Mater. Res. Bull.*, 2013, **48**, 4406–4410.
33 S. Huang, L. Deng, K. Zhou, Z. Hu, S. Sun, Y. Ma and P. Xiao, *J. Magn. Magn. Mater.*, 2012, **324**, 3149–3153.
34 Y. P. Sukhorukov, E. A. Gan'shina, N. N. Loshkareva, A. R. Kaul, O. Y. Gorbenko, A. V. Telegin, S. N. Tugushev, O. V. Mel'nikov and A. N. Vinogradov, *J. Exp. Theor. Phys.*, 2007, **104**, 569–576.
35 W. Ke, N. Zhang, T. Geng and R. Gao, *J. Magn. Magn. Mater.*, 2007, **312**, 430–434.
36 A. Musialik-Piotrowska and H. Landmesser, *Catal. Today*, 2008, **137**, 357–361.
37 O. Y. Gorbenko, O. V. Melnikov, A. R. Kaul, L. I. Koroleva, N. A. Babushkina, A. N. Taldenkov, A. V. Inyushkin, A. Barranco and R. Szymczak, *Thin Solid Films*, 2008, **516**, 3783–3790.
38 Y. Kalyana Lakshmi and P. Venugopal Reddy, *J. Magn. Magn. Mater.*, 2009, **321**, 1240–1245.
39 M. B. Bellakki, C. Shivakumara, N. Y. Vasanthacharya and A. S. Prakash, *Mater. Res. Bull.*, 2010, **45**, 1685–1691.
40 A. Ekber Irmak, A. Coskun, E. Tasarkuyu, S. Akturk, G. Unlu, Y. Samancioglu, C. Sarikurkcu, B. M. Kaynar and A. Yucel, *J. Magn. Magn. Mater.*, 2010, **322**, 945–951.

41 A. Anshul, S. S. Amritphale, S. Kaur, N. Chandra, A. K. Gupta and R. Yadav, *Int. J. Appl. Ceram. Technol.*, 2012, **9**, 214–220.

42 R. Cobas, S. Muñoz-Perez, J. M. Cadogan, T. Puig and X. Obradors, *Appl. Phys. Lett.*, 2011, **99**, 083113.

43 J. X. Wang, J. L. Sun, C. R. He, Q. Wang and W. G. Wang, *J. Power Sources*, 2014, **253**, 424–430.

44 S. K. Bikkarolla, F. Yu, W. Zhou, P. Joseph, P. Cumpson and P. Papakonstantinou, *J. Mater. Chem. A*, 2014, **2**, 14493.

45 S.-A. Park, H. Lim and Y.-T. Kim, *ACS Catal.*, 2015, **5**, 3995–4002.

46 D. C. Higgins, M. A. Hoque, F. Hassan, J.-Y. Choi, B. Kim and Z. Chen, *ACS Catal.*, 2014, **4**, 2734–2740.

47 G. Wu, K. L. More, C. M. Johnston and P. Zelenay, *Science*, 2011, **332**, 443–447.

48 G. Kéranguéven, S. Royer and E. Savinova, *Electrochem. Commun.*, 2015, **50**, 28–31.

49 T. J. Schmidt, V. Stamenkovic, J. P. N. Ross and N. M. Markovic, *Phys. Chem. Chem. Phys.*, 2003, **5**, 400–406.

50 F. Cheng, Y. Su, J. Liang, Z. Tao and J. Chen, *Chem. Mater.*, 2010, **22**, 898–905.

51 X. Ge, A. Sumboja, D. Wuu, T. An, B. Li, F. W. T. Goh, T. S. A. Hor, Y. Zong and Z. Liu, *ACS Catal.*, 2015, **5**, 4643–4667.

52 D. W. Banham, J. N. Soderberg and V. I. Birss, *J. Phys. Chem. C*, 2009, **113**, 10103–10111.

53 N. A. Merino, B. P. Barbero, P. Eloy and L. E. Cadús, *Appl. Surf. Sci.*, 2006, **253**, 1489–1493.

54 S. Ponce, M. A. Peña and J. L. G. Fierro, *Appl. Catal., B*, 2000, **24**, 193–205.

55 J. Hu, L. Wang, L. Shi and H. Huang, *Electrochim. Acta*, 2015, **161**, 115–123.

56 I. Roche, E. Chaînet, M. Chatenet and J. Vondrák, *J. Phys. Chem. C*, 2007, **111**, 1434–1443.

57 A. A. Kulikovsky, *J. Electroanal. Chem.*, 2015, **738**, 130–137.

58 J. Tulloch and S. W. Donne, *J. Power Sources*, 2009, **188**, 359–366.

59 A. S. Ryabova, F. S. Napolskiy, T. Poux, S. Y. Istomin, A. Bonnefont, D. M. Antipin, A. Y. Baranchikov, E. E. Levin, A. M. Abakumov, G. Kéranguéven, E. V. Antipov, G. A. Tsirlina and E. R. Savinova, *Electrochim. Acta*, 2016, **187**, 161–172.

60 Z. Wang, Y. You, J. Yuan, Y. X. Yin, Y. T. Li, S. Xin and D. Zhang, *ACS Appl. Mater. Interfaces*, 2016, **8**, 6520–6528.

61 F. Lu, Y. Wang, C. Jin, F. Li, R. Yang and F. Chen, *J. Power Sources*, 2015, **293**, 726–733.

62 S. Xu, Z. Li, Y. Ji, S. Wang, X. Yin and Y. Wang, *Int. J. Hydrogen Energy*, 2014, **39**, 20171–20182.

63 M. Wang, Y. Lai, J. Fang, J. Li, F. Qin, K. Zhang and H. Lu, *Int. J. Hydrogen Energy*, 2015, **40**, 16230–16237.

64 S. Sun, H. Miao, Y. Xue, Q. Wang, S. Li and Z. Liu, *Electrochim. Acta*, 2016, **214**, 49–55.

65 S. Li, H. Miao, Q. Xu, Y. Xue, S. Sun, Q. Wang and Z. Liu, *RSC Adv.*, 2016, **6**, 99179–99183.

66 E. S. Davydova, I. N. Atamanyuk, A. S. Ilyukhin, E. I. Shkolnikov and A. Z. Zhuk, *J. Power Sources*, 2016, **306**, 329–336.